EFFECT OF CENTRAL MASS CONCENTRATION ON THE FORMATION OF NUCLEAR SPIRALS IN BARRED GALAXIES

PARIJAT THAKUR[1], H.B. ANN[2], AND ING-GUEY JIANG[1]

ABSTRACT

We have performed smoothed particle hydrodynamics (SPH) simulations to study the response of the central kiloparsec region of a gaseous disk to the imposition of nonaxisymmetric bar potentials. The model galaxies are composed of the three axisymmetric components (halo, disk, and bulge) and a non-axisymmetric bar. These components are assumed to be invariant in time in the frame corotating with the bar. The potential of spherical γ-models of Dehnen is adopted for the bulge component whose density varies as $r^{-\gamma}$ near the center and r^{-4} at larger radii and hence, possesses a central density core for $\gamma = 0$ and cusps for $\gamma > 0$. Since the central mass concentration of the model galaxies increases with the cusp parameter γ, we have examined here the effect of the central mass concentration by varying the cusp parameter γ on the mechanism responsible for the formation of the symmetric two-armed nuclear spirals in barred galaxies. Our simulations show that the symmetric two-armed nuclear spirals are formed by hydrodynamic spiral shocks driven by the gravitational torque of the bar for the models with $\gamma = 0$ and 0.5. On the other hand, the symmetric two-armed nuclear spirals in the models with $\gamma = 1$ and 1.5 are explained by gas density waves. Thus, we conclude that the mechanism responsible for the formation of the symmetric two-armed nuclear spirals in barred galaxies changes from the hydrodynamic shocks to the gas density waves when the central mass concentration increases from $\gamma = 0$ to 1.5.

Subject headings: galaxies: evolution — galaxies: kinematics and dynamics — galaxies: nuclei — galaxies: spiral — galaxies: structure — methods: numerical

[1]Department of Physics and Institute of Astronomy, National Tsing-Hua University, Hsin-Chu 30013, Taiwan; pthakur@phys.nthu.edu.tw, jiang@phys.nthu.edu.tw

[2]Division of Science Education, Pusan National University, Busan 609-735, Korea; hbann@pusan.ac.kr

1. INTRODUCTION

High resolution visible and near-infrared observations by the *Hubble Space Telescope (HST)* and ground-based telescopes with adaptive optics show nuclear spirals in the centers of active galaxies (Regan & Mulchaey 1999; Martini & Pogge 1999; Pogge & Martini 2002; Martini et al. 2003a,b), as well as in those of normal galaxies (Phillips et al. 1996; Elmegreen et al. 1998; Laine et al. 1999, 2001; Carollo et al. 2002; Martini et al. 2003a,b). Nuclear spirals have a variety of morphologies such as grand-design spirals, one-armed spirals, and flocculent spirals (Martini et al. 2003a). The grand-design nuclear spirals are symmetric two-armed spirals, while the flocculent, or "chaotic," nuclear spirals have multiple arms that are likely to be segmented into smaller arms.

The morphology of symmetric two-armed nuclear spirals depends on the gas sound speed and the shape of the gravitational potential in the nuclear regions of galaxies (Englmaier & Shlosman 2000; Ann & Thakur 2005). A number of hydrodynamic simulations (Englmaier & Gerhard 1997; Patsis & Athanassoula 2000; Englmaier & Shlosman 2000; Maciejewski et al. 2002; Ann & Thakur 2005) have already been performed to understand the effect of the gas sound speed on the gas flows inside the inner Lindblad resonance (ILR). The smoothed particle hydrodynamics (SPH) simulations of Englmaier & Gerhard (1997) and Patsis & Athanassoula (2000) showed that the off-axis shocks form at low gas sound speed, while the on-axis shocks develop at high gas sound speed. However, they were unable to analyze the nuclear morphology in detail due to the lack of resolution of their simulations. On the other hand, the symmetric two-armed nuclear spirals generated by the gravitational torque of the bar were found in the high-resolution hydrodynamic simulations of Englmaier & Shlosman (2000), Maciejewski et al. (2002), and Ann & Thakur (2005). It was shown by Englmaier & Shlosman (2000) with grid-based hydrodynamic simulations that the symmetric two-armed nuclear spiral can be explained in terms the gas density waves, since the spiral arms open out as the gas sound speed increases. A similar effect of the gas sound speed on the openness of symmetric two-armed nuclear spirals was also found in the SPH simulations of Ann & Thakur (2005). However, their simulations suggested that the symmetric two-armed nuclear spirals are formed by hydrodynamic spiral shocks driven by the bar. Furthermore, Maciejewski et al. (2002) found that the gas sound speed plays a crucial role in the mechanism responsible for the formation of the symmetric two-armed nuclear spirals in barred galaxies. Their grid-based hydrodynamic simulations showed that the symmetric two-armed nuclear spirals are formed by hydrodynamic shocks driven by the bar when the gas sound speed is high ($c_s = 20$ km s^{-1}), while for gas at a low sound speed ($c_s = 5$ km s^{-1}), they are maintained by gas density waves. It was noticed in the grid-based hydrodynamic simulations of Maciejewski (2004) that like the gas sound speed, the bar strength can also affect the mechanism responsible for the formation of the symmetric two-armed nuclear spirals in barred galaxies.

Since the central mass concentration determines the shape of the gravitational potential in the nuclear regions of galaxies, it can also affect the morphology of symmetric two-armed nuclear spirals. This can be understood from the simulations of Englmaier & Shlosman (2000) and Ann & Lee (2004), where they have mentioned that the openness of symmetric two-armed nuclear spiral arms depends on the central mass concentration. Our previous simulations (Ann & Thakur 2005) showed that the presence of a central supermassive black hole (SMBH), which can greatly affect the central mass concentration, plays a significant role in the sense that the symmetric two-armed nuclear spirals form when the mass of an SMBH is massive enough to remove the inner inner Lindblad resonance (IILR). In addition to this, Maciejewski (2004) noticed that a central massive black hole (MBH) of sufficient mass can allow the symmetric two-armed nuclear spirals to extend all the way to its immediate vicinity.

However, it is important to note here that the effect of the central mass concentration on the mechanism responsible for the formation of the symmetric two-armed nuclear spiral was not known from previous studies, whereas that of the gas sound speed was understood from the simulations of Maciejewski et al. (2002). Furthermore, it is worth mentioning that if we consider the model galaxy whose bulge central density varies as $r^{-\gamma}$, its mass would be more centrally concentrated as the cusp parameter γ increases. Thus, the purpose of the present paper is to examine the effect of the central mass concentration by varying the cusp parameter γ on the mechanism responsible for the formation of the symmetric two-armed nuclear spirals in barred galaxies. For this purpose, we employ the SPH technique to solve the hydrodynamic equations for the gas flow in the model galaxies whose bulge central densities vary as $r^{-\gamma}$. We have also included the self-gravity of the gas in our calculations, since this can play a significant role in high-density regions such as shocks.

The remainder of this paper is organized as follows. In § 2 we describe the model galaxy, model parameters, the gaseous disk model, and the numerical method. In § 3 we present the results of our simulations, and the discussion of our results is given in § 4. The conclusions are presented in § 5.

2. MODELS AND NUMERICAL METHODS

2.1. The Model Galaxy

The model galaxy is assumed to be composed of four components: halo, disk, bulge, and bar. The properties (density, size and structure) of all these potential generating components are assumed to be invariant in time in the frame corotating with the bar.

The halo component, which gives rise to the flat rotation curve at outer radii, is assumed to have a logarithmic potential with finite core radius,

$$\Phi(r)_{halo} = \frac{1}{2}v_0^2 \ln(R_h^2 + r^2) + const, \tag{1}$$

where R_h is the halo core radius and v_0 is the constant rotation velocity at large r.

The disk component is assumed to have the potential of Freeman's (1970) exponential disk,

$$\begin{aligned}\Phi(r)_{disk} &= \pi G \Sigma_0 r \left[I_0\left(\frac{r}{2R_d}\right) K_1\left(\frac{r}{2R_d}\right) \right.\\ &\left. - I_1\left(\frac{r}{2R_d}\right) K_0\left(\frac{r}{2R_d}\right) \right],\end{aligned} \tag{2}$$

where R_d is the disk scale length, Σ_0 is the central surface density, and I_0, K_0, I_1, and K_1 are the modified Bessel functions. The total disk mass is simply $M_{disk} = 2\pi\Sigma_0 R_d^2$.

For the bulge component, we adopt the potential of the spherical γ-models of Dehnen (1993),

$$\Phi(r)_{bulge} = \frac{GM_{bulge}}{(2-\gamma)R_b} \left[\left(\frac{r}{r+R_b}\right)^{2-\gamma} - 1 \right], \text{ for } \gamma \neq 2, \tag{3}$$

where M_{bulge} is the total mass of the bulge, R_b is the scale-length, and γ is the cusp parameter that can have a value in between $0 \leq \gamma < 3$. Its corresponding density varies as $r^{-\gamma}$ near the center and r^{-4} at large radii, and hence possesses a central density core for $\gamma = 0$ and cusps for $\gamma > 0$. This bulge with $\gamma = 1.5$ most closely resembles the de Vaucouleurs' $R^{1/4}$-profile (Dehnen 1993) that is known to better represent the bulges of real galaxies. Hereafter, the central mass concentration will be represented by γ, since the central mass concentration of the model galaxies increases with the cusp parameter γ.

The bar is a triaxial component in three dimensions. However, our simulation is restricted to the two-dimensional disk. Thus, we assume the following form of the gravitational potential proposed by Long & Murali (1992) for the bar component:

$$\Phi(r)_{bar} = \frac{GM_{bar}}{2a} \log\left(\frac{x-a+T_-}{x+a+T_+}\right), \tag{4}$$

where $T_{\pm} = \sqrt{[(a \pm x)^2 + y^2 + b^2]}$, and a and b are the needle length and softening length, respectively. The parameter a/b defines the elongation of the bar, which is proportional to the axis ratio $\tilde{a}/\tilde{b}$ of the flattened homogeneous ellipsoid bar of Freeman (1966) when $a/b \geq 2$ (see Fig. 3 of Long & Murali 1992), where $\tilde{a}$ and $\tilde{b}$ are the major and minor axes of a flattened homogeneous ellipsoid bar.

2.2.   Model Parameters

TABLE 1

MODEL PARAMETERS

Model	c_s (km s^{-1})	γ
M1	10.	0.0
M2	10.	0.5
M3	10.	1.0
M4	10.	1.5
M5	15.	0.0
M6	15.	0.5
M7	15.	1.0
M8	20.	0.0
M9	20.	0.5
M10	20.	1.0

We have considered ten models M1-M10, which are listed in Table 1. All these models are defined according to different choices of the gas sound speed c_s and the central mass concentration γ. In this paper, we are mainly interested to examine the effect of the central mass concentration γ on the mechanism responsible for the formation of the symmetric two-armed nuclear spirals in barred galaxies when the gas sound speed is chosen to be $c_s = 10$ km s^{-1} (see § 3.2 and § 3.3). Thus, apart from the models with $\gamma = 0$, 0.5, and 1, an additional model with $\gamma = 1.5$ is considered for the gas sound speed of $c_s = 10$ km s^{-1} (i.e., model M4). However, the models with $\gamma = 0$, 0.5, and 1 are chosen for each of the remaining gas sound speeds of $c_s = 15$ and 20 km s^{-1}. Since the total visible mass of the model galaxies is assumed to be $M_G \sim 4 \times 10^{10}$, the masses of the gas, disk, bulge, and bar components in units of $M_{sc} = 2 \times 10^{11} M_\odot$ are $M_{gas} = 0.002$, $M_{disk} = 0.104$, $M_{bulge} = 0.054$, and $M_{bar} = 0.04$, respectively. Thus, the mass distributions of the model galaxies are chosen to be similar to those of early-type barred galaxies ($\sim$SBa), since the disk-to-bulge mass ratio and the fractional mass of the bar are $M_{disk}/M_{bulge} = 2$ and $M_{bar}/M_G = 0.2$, respectively. The scale lengths of the halo, disk, and bulge are assumed to be $R_h = 15.0$ kpc, $R_d = 3.0$ kpc, and $R_b = 0.25$ kpc, respectively. Furthermore, the bar needle length a, the bar softening length b, the bar pattern speed Ω_p, and the rotation velocity of the halo v_0 are fixed at 3.0 kpc, 1.0 kpc, 42.8 km s^{-1} kpc^{-1}, and 186 km s^{-1}, respectively.

Figure 1 shows the rotation curves and angular frequency curves of the models mentioned in Table 1 that have the central mass concentrations of $\gamma = 0$ and 1. Since the models with constant values of γ have the same mass distribution, we present the rotational curves and angular frequency curves of models M1 and M3 that assume $\gamma = 0$ and 1, respectively. The top left panel of Figure 1 represents the rotational velocities of the halo, disk, bulge, and bar components of model M1 with $\gamma = 0$ as a function of radius, while the top right panel shows the rotational curves of model M3 with $\gamma = 1$. Since the bar is nonaxisymmetric component, its contribution to the rotational velocity is included here after averaging it axisymmetrically (Hasan et al. 1993). As can be seen in the top panels of Figure 1, the rotational velocities in the vicinity of the galactic center are affected by the increase in central mass concentration from $\gamma = 0$ to 1. However, the bottom panels of Figure 1 represent the angular frequencies corresponding to the rotational velocity generated by the axisymmetric components as a function of radius. The adaption of $\Omega_p = 42.8$ km s^{-1} kpc^{-1} places the IILR at the negligible distance from the galactic center, and the outer inner Lindblad resonance (OILR) near 1.3 kpc in model M1 with $\gamma = 0$, whereas it places the single ILR close to 1.5 kpc in model M3 with $\gamma = 1$. Furthermore, the corotation radius (R_{CR}) is found to be around $1.2a$ in models M1 and M3 for the above choice of Ω_p. Since the angular frequency curve reaches high values (larger than Ω_p) at the nucleus for model M1 that considers the central mass concentration of $\gamma = 0$, it suggests that for the assumed values of $M_{bulge} = 0.054$ and $R_b = 0.25$ kpc, the

mass of model M1 with $\gamma = 0$ is sufficiently centrally concentrated (Maciejewski 2003) to weaken the IILR by placing its location at the negligible distance from the galactic center. However, the IILR is completely removed and the angular frequency curve goes to infinity at the galactic center for model M3 with $\gamma = 1$, since the central mass concentration increases from $\gamma = 0$ to 1. Although it is not presented here, we would like to mention that except for the slight difference in the very vicinity of galactic center, the rotation curves of the models with the remaining values of $\gamma = 0.5$ and 1.5 appear to be similar to those of model M3 with $\gamma = 1$. In addition to this, the angular frequency curves of the models with $\gamma = 0.5$ and 1.5 do not greatly differ from those of model M3 with $\gamma = 1$, except for the minor shift in the location of the single ILR.

2.3. The Gaseous Disk Model

In the direction of modeling the response of the gaseous disk to the imposition of nonaxisymmetric bar potentials, many significant results have been produced so far when the gas is isothermal (eg., Englmaier & Gerhard 1997; Fukuda et al. 1998, 2000; Fux 1999, 2001; Lee et al. 1999; Patsis & Athanassoula 2000; Englmaier & Shlosman 2000; Ann 2001; Maciejewski et al. 2002; Maciejewski 2003, 2004; Ann & Lee 2004; Ann & Thakur 2005; Perez 2008; Namekata et al. 2008). Englmaier & Gerhard (1997), Englmaier & Shlosman (2000), and Maciejewski (2003) pointed out that this approach of considering isothermal gas is consistent with the ISM model of Cowei (1980), who argued that the cloud fluid can be treated like an isothermal gas if the clouds have an equilibrium mass spectrum. The equilibrium is assumed to be maintained by a steady supply of small clouds by supernovae. Thus, we assume the infinitesimally thin and isothermal uniform gaseous disks with the effective sound speeds of $c_s = 10$, 15, and 20 km s^{-1}. The mass of the gaseous disk was chosen to be 1% of the total visible mass of the model galaxy, since we simulate the response of the central kiloparsec region of the gaseous disk in early-type barred galaxies. In order to represent the initial gaseous disk with constant density, 2×10^4 SPH particles are distributed uniformly over a grid inside a circular disk of 5 kpc radius. The initial circular velocities are given to the SPH particles so that the centrifugal accelerations of the particles are balanced with their gravitational accelerations. In the context of this equilibrium gaseous disk model, the pressure gradient forces are zero. The initial resolution length, defined by equation (12), was found to be ~ 147 pc. However, the resolution of the SPH simulations becomes far better than the initial values in the central region as the density in the nuclear region increases within a few bar rotation periods (see § 2.4). We introduce the bar potential slowly within one-half bar rotation period to avoid a spurious response of the gaseous disk, where the bar rotation period τ_{bar} is $\sim 1.44 \times 10^8$ yr. The previous simulations of the isother-

mal gas flow in barred galaxies with broad spectrum of values for effective sound speed (Englmaier & Gerhard 1997; Patsis & Athanassoula 2000; Maciejewski et al. 2002) and the compilation of HI velocity dispersion by Kamphuis (1993) suggest that our adopted values of $c_s = 10$, 15, and 20 km s^{-1} correspond to the vertical cloud velocity dispersion in the Galactic bulge.

2.4. Numerical Method

We have used the PMSPH method to solve the hydrodynamical equations for the gas flow in barred galaxies. Our simulations are confined in two dimensions, since restricting the calculation to two dimensions increases greatly the resolution, which is important in the present problem of resolving the shocks (cf. Englmaier & Gerhard 1997). In this regard, Englmaier & Gerhard (1997) mentioned that the two-dimensional description appears to be a reasonable approximation, since they have done some three-dimensional simulations, where the gas flows were indeed similar to the two-dimensional ones. We have used the PMSPH code of Fux (1999, 2001), which has recently been used by Perez (2008) to model the gas flow in the barred galaxy NGC 4123. R. Fux of Geneva Observatory Group has kindly provided the PMSPH code to us. Here we briefly describe the necessary specifications relevant to the particular aspects of our PMSPH code and refer the readers to Fux (1999, 2001) for a detailed description of our code and to Benz (1990), Monaghan (1992), and Steinmetz (1996) for the general properties of solving Euler's equation of motion using the popular Lagrangian method.

2.4.1. Gas Hydrodynamics with SPH

Since SPH is fully Lagrangian, it does not have any grid to impose any artificial restrictions on the global geometry of the systems under study or any mesh-related limitations on the dynamic range in spatial resolution. Thus, a high numerical resolution is naturally achieved in high-density regions such as shocks by using SPH (Fukuda et al. 1998), which is necessary to solve our present problem of understanding the response of gaseous disks in the nuclear regions of barred galaxies.

Using the SPH method, we solve the Euler equation of motion that can be written as

$$\frac{d\mathbf{v}}{dt} \equiv \frac{\partial \mathbf{v}}{\partial t} + (\mathbf{v} \cdot \nabla)\mathbf{v} = -\frac{\nabla(P + \Pi)}{\rho} - \nabla\Phi, \tag{5}$$

where $\mathbf{v}(\mathbf{r})$ is the velocity field and $\rho(\mathbf{r})$, $P(\mathbf{r})$ and $\Pi(\mathbf{r})$ are the density, pressure, and artificial

viscosity of the gas, respectively. $-\nabla\Phi$ is the gravitational force, where Φ includes potentials of the gas, as well as the stellar and dark components.

In SPH, the density is evaluated directly at each particle position $\mathbf{r}_i$ in space by summing the contributions from the density profiles of neighboring particles and is represented by

$$\rho_i \equiv \rho(\mathbf{r}_i) = \sum_{j=1}^{N_g} m_j W(\mathbf{r}_i - \mathbf{r}_j, h), \tag{6}$$

where N_g is the number of gas particles, m_j is the mass of individual particles, $W(\mathbf{r}, h)$ is the kernel function, and h is the smoothing length that defines the local spatial resolution and is proportional to the local mean interparticle spacing. In our code, the adopted SPH kernel is a spherically symmetric spline that vanishes outside $2h$ because of its finite spatial extension.

Our code assumes an isothermal equation of state, i.e.,

$$P_i = c_s^2 \rho_i, \tag{7}$$

where c_s is the effective sound speed, which can be interpreted globally as the velocity dispersion of the interstellar clouds. The internal energy of the gas is at any time and everywhere constant, and in particular, there is no energy equation involved in our code. With the above equation (7), the pressure gradient term of Benz (1990) in the Euler's equation simply takes the form

$$\left(\frac{\nabla P}{\rho}\right)_i \approx c_s^2 \sum_{j=1}^{N_g} m_j \left(\frac{1}{\rho_i} + \frac{1}{\rho_j}\right) \nabla_i W(\mathbf{r}_i - \mathbf{r}_j, h). \tag{8}$$

The introduction of an artificial viscosity is required for an accurate treatment of the flow near shocks. In our code, the artificial viscosity is calculated exactly as in Benz (1990). It consists of the bulk and the von Neumann-Richtmyer viscosities, with the standard parameters set to $\alpha = 1.0$ and $\beta = 2.5$, and takes into account Balsara's (1995) correction to avoid energy dissipation in pure shearing flows.

In order to achieve high resolution, it is necessary to treat the smoothing length h properly, since it determines the local spatial resolution. To increase the resolution in high-density regions like shocks, our code uses a spatially variable smoothing length h to assign an individual smoothing length h_i to each particle in such a manner that the number of neighbor particles N_i to each particle always remains as close as possible to a fixed number N_o. This allows us to save significant computing time while keeping spatial resolutions high

enough to resolve the shocks (Fux 1999, 2001). Two particles i and j are defined as mutual neighbors if $i \neq j$ and $|\mathbf{r}_i - \mathbf{r}_j| < 2h_{ij}$, where $h_{ij} = (h_i + h_j)/2$ is the symmetrized smoothing length, which is supplied in equations (6) and (8), as well as in the formula for the artificial viscosity to ensure momentum conservation.

At each time step, the smoothing lengths are updated in our code according to the general three-dimensional scaling law:

$$\frac{h_i}{h_o} = \left(\frac{N_i + 1}{N_o + 1} \frac{\rho_o}{\rho_i} \right)^{1/3}, \tag{9}$$

where h_o and ρ_o are constants, N_i is the number of neighbors of particle i, and $+1$ is added to take into account particle i. Following Benz (1990), we take the time derivative of equation (9) and substitute the continuity equation to yield

$$\dot{h}_i \equiv \frac{dh_i}{dt} = \frac{1}{3} h_i \left(\frac{1}{N_i + 1} \frac{dN_i}{dt} + [\nabla \cdot \mathbf{v}]_i \right). \tag{10}$$

In equation (10), Benz (1990) did not include the term dN_i/dt to ensure a constant number of neighbors. However, this does not prevent a slow numerical departure of the N_i's from N_o with time. To overcome this problem, our code simply damps such departures by setting

$$\frac{dN_i}{dt} = \frac{N_i - N_o}{\eta \triangle t} \tag{11}$$

in equation (10) and integrates the resulting equation along with the equations of motion. The parameter η controls the damping rate per time step $\triangle t$ and should be significantly greater than 1 to avoid abrupt discontinuities in nongravitational forces. In all our simulations, we have assumed $N_o = 35$ and $\eta = 5$.

The initial smoothing lengths of the gas particles, confined near the plane $z = 0$, are defined as

$$h_i(t = t_o) = \sqrt{\frac{N_o m_i}{4\pi \Sigma(R_g)}}, \tag{12}$$

where m_i and $\Sigma(R_g)$ are the mass of each gas particle and the surface density of the initial gaseous disk of radius $R_g = 5$ kpc, respectively.

It is customary to impose quite a large lower limit on the minimum smoothing length h_{min} to save computing time. However, because of the fast neighbor searching algorithm adopted in our code, we have used $h_{min} = 0.1$ pc to resolve structures down to the parsec scale. Although the initial smoothing length (i.e., the initial resolution length) of ~ 147 pc is employed in our simulations (see § 2.3), the smallest smoothing length actually achieved

after a few bar rotation periods is ~ 2 pc, which is smaller than the $h_{min} = 5$ pc used in the high-resolution SPH simulations of Fukuda et al. (2000). We find that the smoothing length of ~ 2 pc is small enough to resolve the nuclear spirals, as shown in § 3. Furthermore, it is worth mentioning here that our code uses a synchronized version of the standard leap-frog time integrator (e.g., Hut et al. 1995), which is known to well conserve the total energy and the total angular momentum and also employs an adaptive time step to temporally resolve the high-density shocks in the gaseous disk (see Fux 1999, 2001).

2.4.2. Gravitation with PM

Our gaseous disk is not a self-gravitating one, since its mass is assumed to be only a tiny fraction of the model galaxy ($\sim 1\%$). This suggests that Toomre's Q value is much greater than unity (i.e., $Q >> 1$), which represents a stable gaseous disk (cf. Elmegreen & Thomasson 1993; Fukuda et al. 1998, 2000; Ann & Thakur 2005). However, we have included the self-gravity of gas in our calculations because it can play a significant role in high-density regions such as shocks that develop in the later evolution of gaseous disk. To compute to the self-gravity of gas, our code uses the particle-mesh (PM) technique with polar-cylindrical grid geometry described in Pfenniger & Friedli (1993). The advantage of considering the polar-cylindrical grid is that the radial and azimuthal resolutions increase toward the center, where a variety of features are likely to develop because of the gas inflow driven by the bar. Using the convolution theorem, the potential is computed on the polar-cylindrical grid by the fast Fourier transform (FFT) technique in the ϕ and z dimensions, where the cells are equally spaced. The radial spacing of the cells is logarithmic with a linear core to avoid an accumulation point at the center. Since the Keplerian kernel does not truly satisfy the conditions of the convolution theorem, a variable homogeneous ellipsoidal kernel is adopted in our code for the softening of the short range forces (cf. Pfenniger & Friedli 1993; Fux 1999, 2001). This kernel tends toward the Keplerian kernel at large distance, and can also be useful in situations that need anisotropic resolution (Pfenniger & Friedli 1993). Since the polar-cylindrical grid is non-homogeneous, a variable softening length is necessary. Otherwise a softening length intermediate between the smallest and largest cell sizes both decreases resolution in some parts of the grid and enhances grid noise in other parts of the grid. Thus, the softening lengths represented by the semi-axes of our adopted variable homogeneous ellipsoidal kernel have been set as 1.1 times the respective cell dimensions. This ensures the conservation of the total energy, as well as of the total angular momentum while keeping high central resolution (Pfenniger & Friedli 1993; Fux 1999, 2001). For a more detailed description of the PM technique used in our code, we simply refer the readers to Pfenniger & Friedli (1993) and Fux (1999, 2001).

3. RESULTS

3.1. Nuclear Feature of the Gaseous Disk

The nuclear features of the gaseous disks in models M1-M10 at the evolution time of $10\tau_{bar}$ are shown in Figure 2. Here our results are shown on the frame corotating with the bar, which always lies horizontally. As can be seen in Figure 2, models M1-M10 clearly show the development of symmetric two-armed nuclear spirals at the evolution time of $10\tau_{bar}$. For models M1-M4 in the first column that consider the gas sound speed of $c_s = 10$ km s^{-1}, the innermost parts of the symmetric two-armed nuclear spiral of model M1 with $\gamma = 0$ extend up to winding angle of $\sim \frac{9}{4}\pi$, whereas they can wind up to $\sim 2\pi$ for model M4 with $\gamma = 1.5$. It is also apparent that the nuclear disks are completely filled with the gas particles for models M8-M10 in the last column that assume the gas sound speed of $c_s = 20$ km s^{-1}. In this case, the innermost parts of the symmetric two-armed nuclear spiral of model M8 with $\gamma = 0$ extend all the way to the center with winding angle of $\sim 3\pi$, whereas they appear to be tightly wound in the sense that their arms cannot be resolved after $\sim \frac{5}{2}\pi$ for model M10 with $\gamma = 1$. These characteristics of the nuclear features show that the symmetric two-armed nuclear spiral arms open out as the central mass concentration γ decreases while keeping the gas sound speed c_s constant. By comparing the winding angles corresponding to the symmetric two-armed nuclear spirals of the models with constant values of γ in Figure 2 such as those mentioned above for models M1 and M8 that assume $\gamma = 0$ but different gas sound speeds of $c_s = 10$ and 20 km s^{-1}, respectively, it is clear that the nuclear spiral arms also open out as the gas sound speed c_s increases while keeping the central mass concentration γ constant. In addition to the above nuclear features of the gaseous disks in models M1-M10, Figure 2 also shows that the diameter of the nuclear disk depends on the central mass concentration γ and the gas sound speed c_s. The models with high central mass concentrations allow a larger nuclear disk than those with low central mass concentrations. Furthermore, a larger nuclear disk is also found in the models with low gas sound speeds. As a result, a largest nuclear disk among our selected models is noticed in model M4, which assumes $\gamma = 1.5$ and $c_s = 10$ km s^{-1}.

3.2. Nuclear Distribution of the Shocked Gaseous Particles

As shown in the previous section, all the models in the present study show the formation of the symmetric two-armed nuclear spirals at the evolution time of $10\tau_{bar}$. The mechanisms such as the hydrodynamic shocks (Maciejewski et al. 2002; Ann & Thakur 2005) and the gas density waves (Englmaier & Shlosman 2000) were proposed for the formation of such nuclear

spirals in barred galaxies. Since a significant role is played by the gas sound speed c_s to decide whether the symmetric two-armed nuclear spirals are formed by hydrodynamic shocks or by gas density waves (cf. Maciejewski et al. 2002), we are interested here to examine any such role of the central mass concentration γ. For this study, we mainly consider models M1-M4, which have $c_s = 10$ km s^{-1} but different central mass concentrations of $\gamma = 0$, 0.5, 1, and 1.5, respectively. In order to see whether the symmetric two-armed nuclear spirals shown in Figure 2 for models M1-M4 are made of shocked gas particles, we examine the distributions of gas particles that are shocked by supersonic flow, i.e., $-h\nabla \cdot v > c_s$ (Englmaier & Gerhard 1997; Ann & Thakur 2005), in the central kiloparsec of models M1-M4 at the evolution time of $10\tau_{bar}$ in Figure 3. As can be seen in Figure 3, the distributions of shocked gas particles in the central kiloparsec of models M1 and M2 reveal well-defined spiral patterns whose innermost parts extend up to winding angle of $\sim 2\pi$. These nuclear spiral shocks look very similar to the symmetric two-armed nuclear spiral patterns developed in Figure 2 for the distributions of all the gas particles in the central kiloparsec of models M1 and M2. On the other hand, it is also apparent from Figure 3 that the distributions of shocked gas particles in the central kiloparsec of models M3 and M4 cannot move inward in a curling manner after winding angle of π. However, the distributions of all the gas particles in the central kiloparsec of models M3 and M4 show the development of symmetric two-armed nuclear spirals whose innermost parts extend up to winding angle of $\sim 2\pi$, as shown in Figure 2. Thus, our simulations suggest that the symmetric two-armed nuclear spirals of models M1 and M2 that respectively assume $\gamma = 0$ and 0.5 are formed by hydrodynamic spiral shocks driven by the gravitational torque of the bar, whereas they cannot be supported by the shocked gas particles for models M3 and M4 that respectively assume $\gamma = 1$ and 1.5. It is worthwhile to mention here that the models with each of the remaining values of the gas sound speed (i.e., $c_s = 15$ and 20 km s^{-1}) show a similar effect of the central mass concentration γ on the formation of the nuclear spirals in barred galaxies to that shown in Figure 3 for the models with $c_s = 10$ km s^{-1}.

3.3. Effect of Central Mass Concentration on Gas Inflow

Symmetric two-armed nuclear spirals are suggested to be formed by the gas inflow across the ILR due to the loss of angular momentum at the shocks driven by the gravitational torque of the bar (Maciejewski 2003, 2004; Ann & Thakur 2005). Thus, it is quite plausible that the central mass concentration γ can affect the gas inflow into central hundred parsec of models M1-M4 with $c_s = 10$ km s^{-1}, since Figure 3 shows that the central mass concentrations of $\gamma = 0$ and 0.5 make physical conditions in which it is plausible for the symmetric two-armed nuclear spirals to take the form of hydrodynamic shocks. This inspires us to examine the

effect of the central mass concentration γ on the gas inflow into the central hundred parsec of models M1-M4 in detail. In order to do this, the time evolution of the fraction of gas particles accumulating inside the radial zone of 0.3 kpc is shown in Figure 4 for models M1-M4. The gas accumulated inside the radial zone of 0.3 represents the gas inflow deep inside the ILR, since the OILR in model M1 and the ILRs in models M2-M4 are located around at 1.3 kpc and 1.5 kpc, respectively. As can be seen in Figure 4, models M1-M4 show appreciable gas inflow into the central hundred parsec throughout the evolution. Although there are little differences in the gas inflow among the models in the early phase of evolution, model M4 with $\gamma = 1.5$ shows slightly larger gas inflow up to $\sim 6\tau_{bar}$. However, at the later evolution times (i.e., after $\sim 6\tau_{bar}$), the remarkable differences in the gas inflow are found in the sense that the gas inflow increases as the central mass concentration decreases from $\gamma = 1.5$ to 0. As a result, the highest gas inflow rate is found for model M1 with $\gamma = 0$ whose mass is less centrally concentrated than models M2-M4 that assume $\gamma = 0.5$, 1 and 1.5, respectively. This correlation between the amount of gas inflow close to the center and the central mass concentration still exists when the models with each of the remaining values of the gas sound speed (i.e., $c_s = 15$ and 20 km s^{-1}) are considered. However, similar to Patsis & Athanassoula (2000) and Ann & Thakur (2005), the gas inflow rate increases when the gas sound speed increases from $c_s = 10$ to 20 km s^{-1}.

4.   DISCUSSION

4.1.   Dependence of Gas Flow Morphology on Central Mass Concentration and Gas Sound Speed

Using the SPH method, Englmaier & Gerhard (1997) have found that when the gas in barred galaxies is modelled as an isothermal fluid, the gas flow morphology depends on the shape of the underlying potential and the sound speed. They noticed that the off-axis principal shocks with a nuclear ring developed by the gas flow at low sound speed turn into the on-axis ones with a straight inflow to the center when the sound speed is high. However, the resolutions of their simulations were not high enough to analyze the nuclear morphology in detail. Our present SPH simulations confirm their findings that not only the underlying potential, which can be greatly affected by the central mass concentration, but also the gas sound speed influence the morphology of the gas flow.

Because of the better resolution of our SPH simulations, we analyze the gas flows in the central kiloparsecs of barred galaxies, where the morphology of nuclear spirals is found to be dependent on the central mass concentration γ and the gas sound speed c_s (see § 3.1). The openness of the nuclear spiral arms increases as the central mass concentration decreases.

Increasing the gas sound speed has a comparable effect on the openness of nuclear spirals to that of decreasing the central mass concentration. This implies that the nuclear spiral arms also open out when the gas sound speed increases. As a result, the less centrally concentrated model with high gas sound speed (i.e., model M8 with $\gamma = 0$ and $c_s = 20$ km s^{-1}) shows more loosely wound nuclear spiral whose openness appears to be larger than those of the other selected models. This can be justified by the fact that the innermost parts of the nuclear spiral formed in model M8 extend all the way to the galactic center with winding angle of $\sim 3\pi$ (see § 3.1 and Fig. 2). A similar effect of the central mass concentration and the gas sound speed on the morphology of nuclear spirals was found by Englmaier & Shlosman (2000), although they used the two-dimensional grid-based hydrodynamics code ZEUS-2D. In addition to this, Maciejewski et al. (2002), who use the grid-based hydrodynamics code, have also found that the nuclear spiral opens out in the sense that its innermost parts reach very close to the galactic center when the gas sound increases from $c_s = 5$ to 20 km s^{-1}.

Ann & Thakur (2005), who use the SPH code, have found that the models with lower gas sound speeds allow a larger diameter of the nuclear disk than those with high gas sound speeds. Here we have also found a similar effect of the gas sound speed on the diameter of the nuclear disk (see § 3.1 and Fig. 2). Beside this, we have noticed that the diameter of the nuclear disk increases as the central mass concentration γ increases. A similar effect of the central mass concentration and the gas sound speed on the diameter of the nuclear disk has been found by Englmaier & Shlosman (2000). Thus, it is apparent that increasing the central mass concentration has a similar effect on the diameter of the nuclear disk to that of decreasing the gas sound speed.

Furthermore, it was also found by Ann & Thakur (2005) that the nuclear regions of the modeled gaseous disks evolve to trailing nuclear spirals whose morphologies depend on the gas sound speed in the presence of a central SMBH that is massive enough to remove the IILR, whereas the lower gas sound speed model ($c_s = 10$ km s^{-1}) that has the existence of the IILR due to the absence of a central SMBH evolves to a leading nuclear spiral. In general, the leading nuclear spirals are generated at the IILR because of the positive torque of the bar (Combes et al. 2002), while the trailing nuclear spirals at the OILR (or at the ILR when there is no IILR) are made by orbital switching from the x_1-orbits that align with the bar axis to the x_2-orbits perpendicular to the bar (Athanassoula 1992; Wada 1994; Knapen et al. 1995; Englmaier & Shlosman 2000). We have not seen here any such existence of the leading nuclear spirals, since the masses of models with $\gamma = 0$ are sufficiently centrally concentrated to weaken the IILR by placing its location at the negligible distance from the galactic center (see Fig. 1). This makes physical conditions plausible for the development of trailing nuclear spirals in the models with $\gamma = 0$ whose innermost parts can reach the galactic center when the gas sound speed is high (see Fig. 2). A similar dependence of the

morphology of trailing nuclear spirals on the gas sound speed was found for the models with $\gamma \geq 0.5$ that have only a single ILR due to the increase of central mass concentration from $\gamma = 0$.

The relative bar strength is important in galaxy morphological studied because phenomena such as the gas inflow can be affected in various ways to the effectiveness with which the bar potential influences the motion of gas in a galactic disk (eg., Selloow & Wilkinson 1993; Buta & Combes 1996; Knapen 1999). As mentioned in Block et al. (2001), the relative bar strength defined by the maximum of the tangential-to-radial force ratio $(F_{Tan}/F_{Rad})_{max}$ increases when the bulge becomes weak. We have found here that the gas inflow into the central hundred parsec increases as the central mass concentration decreases from $\gamma = 1.5$ to 0 (see § 3.3 and Fig. 4). This correlation between the amount of gas inflow close to the center and the central mass concentration can be understood if we consider the dependence of the relative bar strength $(F_{Tan}/F_{Rad})_{max}$ on the strength of the bulge. Since the relative bar strength $(F_{Tan}/F_{Rad})_{max}$ increases as the bulge becomes weak with the decrease in central mass concentration γ, the gravitational torques of the bars would be stronger in the models with $\gamma = 0$ than in the models with $\gamma = 1.5$. This provides favorable conditions for the gas particles in the models with $\gamma = 0$ to lose their angular momentum much faster than those in the models with $\gamma = 1.5$. Thus, the highest gas inflow rate is found for model M1 with $\gamma = 0$ (see § 3.3 and Fig. 4), since the gas particles move inward because of the loss of angular momentum. Apart from the relative bar strength, the gas inflow close to the center can also be understood by the ILR that exists only if the central mass concentration is large enough (Englmaier & Gerhard 1997; Patsis & Athanassoula 2000; Englmaier & Shlosman 2000). The ILR is defined as the outer limit to which the x_2-orbits can extend (Maciejewski 2004). If the ILR is absent, the x_2-orbits do not exist, and strong gas inflow to the center can take place (Athanassoula 1992; Piner et al. 1995). As can be seen in Figure 2, decreasing the central mass concentration from $\gamma = 1.5$ to 0 corresponds to the decrease in the strength of the ILR in the sense that the diameter of the nuclear disk, which represents the region occupied by the x_2-orbits, decreases (cf. Englmaier & Shlosman 2000). This causes the highest gas inflow rate in the less centrally concentrated model (eg., model M1 with $\gamma = 0$), as suggested by Englmaier & Shlosman (2000).

Using the SPH method, Patsis & Athanassoula (2000) and Ann & Thakur (2005) have found that the gas inflow inside the radial zone near the central regions increases with the gas sound speed. In addition to this, some previous simulations, which either use the SPH code (Englmaier & Gerhard 1997) or the grid-based hydrodynamics code (Englmaier & Shlosman 2000; Maciejewski et al. 2002; Maciejewski 2004), also indicate that the gas inflow close to the center increases with the gas sound speed. Although we have only presented here the effect of the central mass concentration on the gas inflow, a closer look at Figure 2 suggests

a similar correlation between the amount of gas inflow close to the center and the gas sound speed to that found in previous simulations. This can be understood if we consider the findings of Patsis & Athanassoula (2000) and Englmaier & Shlosman (2000) that while the gas particles in the low sound speed mediums easily follow the x_2-orbits, the gas particles in the high sound speed mediums face more difficulty doing so. Because of this reason, Figure 2 shows that the diameter of the nuclear disk, which represents the region occupied by the x_2-orbits, decreases when the gas sound speed increases from $c_s = 10$ to 20 km s^{-1} (cf. Englmaier & Shlosman 2000), resulting in a large amount of gas inflow deep inside the ILR for the models with high gas sound speed ($c_s = 20$ km s^{-1}). Thus, the above described correlations make physical conditions in which it is plausible for the innermost parts of nuclear spiral to reach very close to the center when the less centrally concentrated model with high gas sound speed is considered (see Fig. 2).

4.2. Mechanism Responsible for the Formation of Nuclear Spirals

The gas density waves (Englmaier & Shlosman 2000; Maciejewski et al. 2002) and the hydrodynamic shocks (Maciejewski et al. 2002; Ann & Thakur 2005) are two promising mechanisms proposed for the formation of the symmetric two-armed nuclear spirals in barred galaxies. As mentioned in Englmaier & Shlosman (2000) and Maciejewski et al. (2002), the linear theory of gas density wave postulates the following: (1) the spiral pattern opens out as the gas sound speed increases; (2) the spiral pattern does not extend beyond the IILR when two ILRs are present; (3) when one ILR is present, the spiral pattern can exist between the center and the ILR. Since the gas density waves cannot propagate in regions where shocks are strong enough to drive a nonlinear response of gas flows, it can be applied to low-amplitude spirals where no shocks exist and the gas response can be considered a linear wave (Englmaier & Shlosman 2000; Maciejewski et al. 2002). However, it is worthwhile to mention that the gas density wave itself is triggered by the spiral shocks driven by the gravitational torque of the bar (Englmaier & Shlosman 2000).

The grid-based hydrodynamic simulations of Maciejewski et al. (2002) show that the gas sound speed plays a significant role to decide whether the nuclear spirals are formed by gas density waves or by hydrodynamic shocks. In their low gas sound speed run ($c_s = 5$ km s^{-1}), the nuclear spiral is weak and rather tightly wound that creates at most a factor of 2 density enhancement over the interarm region. Moreover, it terminates just outside the IILR, and its shock strength, as measured by div^2**v** for div **v** < 0, is 10 times smaller than that of the principal shock. This suggests that the nuclear spiral in their low gas sound speed run ($c_s = 5$ km s^{-1}) can be well understood in terms of the gas density waves. On the other

hand, the strong shock nature of nuclear spiral is found by Maciejewski et al. (2002) in their high gas sound speed run ($c_s = 20$ km s^{-1}). They have found that the strong loosely wound nuclear spiral is a direct continuation of the principal shock along the leading edge of the bar, which generally agrees with the linear theory of gas density wave that postulates a open nuclear spiral for a high gas sound speed (cf. Englmaier & Shlosman 2000). Nevertheless, the nuclear spiral reaches close to the nucleus well beyond the IILR where the gas density waves cannot penetrate. In addition to this, the shock strength (i.e., div^2**v** for div **v** < 0) and the arm/interarm density contrast of the nuclear spiral are comparable to those of the principal shocks. This indicates that the nuclear spiral in their high gas sound speed run ($c_s = 20$ km s^{-1}) is definitely well beyond the linear regime explored in the density wave theory where sound waves cannot propagate in regions for which shocks are strong. Our previous SPH simulations in the high sound speed mediums (Ann & Thakur 2005) also show the strong shock nature of nuclear spirals. In these simulations, we have found that the symmetric two-armed nuclear spirals are formed by hydrodynamic shocks in the presence of a central SMBH that can remove IILR when the gas sound speed is high enough to drive a large amount of gas inflow deep inside the ILR.

Like the role of gas sound speed as described above (cf. Maciejewski et al. 2002; Ann & Thakur 2005), we have found here that the central mass concentration also play a significant role in the mechanism responsible for the formation of the symmetric two-armed nuclear spirals in barred galaxies. Our present SPH simulations show that the symmetric two-armed nuclear spiral arms open out as the gas sound speed increases (see § 3.1 and § 4.1), which generally agrees with the predictions of the linear theory of gas density wave. Nevertheless, the symmetric two-armed nuclear spirals of the models with $\gamma = 0$ and 0.5 cannot be explained by gas density waves, since they are supported by the gas particles that are shocked by supersonic flow (see § 3.2 and Fig. 3). On the other hand, since the symmetric two-armed nuclear spirals of the models with $\gamma = 1$ and 1.5 cannot be explained by the shocked gas particles (see § 3.2 and Fig. 3) and their arms open out when the gas sound speed increases, they can be well understood in terms of the gas density waves. This suggests that the symmetric two-armed nuclear spirals formed by hydrodynamic shocks turn into those explained by gas density waves when the central mass concentration increases from $\gamma = 0$ to 1.5. Since the relative strength of bars in the models with $\gamma = 0$ is stronger than that in the models with $\gamma = 1.5$ (see § 4.1), our results appear to confirm the findings of the grid-based hydrodynamic simulations of Maciejewski (2004) that the nuclear spirals developed in the models with strong bars have the nature of shocks in gas, whereas those formed in the models with weak ovals can be explained in terms of the gas density waves. In addition to this, Maciejewski (2004) seems to support our findings that the nuclear spirals formed by hydrodynamic shocks trigger a large amount of gas inflow than those explained in terms of

the gas density waves.

Although our present SPH simulations and the grid-based hydrodynamic simulations of Englmaier & Shlosman (2000) show a similar effect of the central mass concentration and the gas sound speed on the morphology of nuclear spirals (see § 4.1), the shock nature of nuclear spiral was not found by Englmaier & Shlosman (2000). They have found the low-amplitude nuclear spirals, which can be explained by gas density waves because the spiral arms open out as the gas sound speed increases. On the other hand, we have found here that the nuclear spirals can be formed either by hydrodynamic shocks or by gas density waves, depending on the value of central mass concentration γ. It appears that the different assumptions of the mass models along with the adoption of the different hydrodynamics codes might play some role in creating this discrepancy between our present simulations and those of Englmaier & Shlosman (2000).

4.3.   Effect of Number of Particles

After performing the SPH simulations with 2×10^4 and 1×10^5 SPH particles for the response of the gaseous disk to the imposition of nonaxisymmetric bar potentials, Patsis & Athanassoula (2000) claimed that the morphology of gas inflow does not depend on the number of SPH particles for N_g larger than 2×10^4. This encourages us to check whether the number of SPH particles causes any major changes in our results discussed in the previous sections. Thus, we have repeated our simulations for models M1-M10 with 1×10^6 SPH particles that give the initial resolution of ~ 20 pc. Since we are mainly interested to examine whether the number of SPH particles affects our results discussed in §§ 3.2 and 4.2 regarding the role of the central mass concentration γ in the mechanism responsible for the formation of the nuclear spirals in barred galaxies, we have presented here the nuclear distributions of supersonically shocked gas particles (i.e., $-h\nabla \cdot \upsilon > c_s$) for models M1-M4 with 1×10^6 SPH particles at the evolution time of $10\tau_{bar}$ in Figure 5. Similar to Figure 3 that depicts the nuclear distributions of supersonically shocked gas particles for models M1-M4 with 2×10^4 SPH particles at the evolution time of $10\tau_{bar}$, Figure 5 also shows that the nuclear spirals formed in models M1 with $\gamma = 0$ and M2 with $\gamma = 0.5$ have the nature of hydrodynamic shocks in gas, whereas those developed in models M3 with $\gamma = 1$ and M4 with $\gamma = 1.5$ are not supported by the shocked gas particles. Although it is not presented in this paper, the results of our simulations, which employ 1×10^6 SPH particles, are similar to those obtained in the previous sections using 2×10^4 SPH particles for the effect of the central mass concentration γ and the gas sound speed c_s on the morphology of nuclear spirals (see § § 3.1 and 4.1), as well as on the gas inflow close to the center (see § § 3.3 and

4.1). This implies that similar to our simulations with 2×10^4 SPH particles (see § § 3.1 and 4.1), the nuclear spiral arms formed in all the models with 1×10^6 SPH particles also open out as the gas sound speed c_s increases. Because of this fact, our simulations with 1×10^6 SPH particles suggest that the nuclear spirals of models M3 with $\gamma = 1$ and M4 with $\gamma = 1.5$ can be explained in terms of the gas density waves (cf. Englmaier & Shlosman 2000), which is consistent with the formation mechanism proposed in § 4.2 for the nuclear spirals of these models with 2×10^4 SPH particles. As a result, we do not see any changes in our findings regarding the effect of the central mass concentration γ on the mechanism responsible for the formation of the nuclear spirals in barred galaxies when the number of SPH particles increases from 2×10^4 to 1×10^6. From this, we can conclude that similar to Patsis & Athanassoula (2000), our results do not depend on the number of SPH particles for N_g larger than 2×10^4, and thus that this number of SPH particles is sufficient to examine the shock nature of nuclear spirals in barred galaxies.

5. CONCLUSIONS

We have used the SPH method to find the response of the nuclear region of a gaseous disk to the imposition of nonaxisymmetric bar potentials in order to understand the effect of the central mass concentration γ on the mechanism responsible for the formation of the symmetric two-armed nuclear spirals in barred galaxies. We have found that the central mass concentration γ plays a significant role in shaping the gravitational potential in the central kiloparsec to weaken or to remove the IILR that prevents the gas inflow close to the nucleus. It was also noticed that the gas flow driven by the gravitational torque of the bar leads to the formation of symmetric two-armed nuclear spiral whose morphology depends on the central mass concentration γ and the gas sound speed c_s in the sense that the nuclear spiral arms open out when either the central mass concentration decreases or the gas sound speed increases. Thus, the less centrally concentrated model with high gas sound speed shows more loosely wound nuclear spiral whose innermost parts reach the galactic center in a curling manner. A largest nuclear disk is found for the more centrally concentrated model with low gas sound speed.

Furthermore, the central mass concentration γ is found to play a crucial role to decide whether the symmetric two-armed nuclear spirals are formed by hydrodynamic shocks or by gas density waves. The symmetric two-armed nuclear spirals are formed by hydrodynamic spiral shocks caused by the gravitational torque of the bar for the models with $\gamma = 0$ and 0.5, whereas they are explained in terms of the gas density waves when the models with $\gamma = 1$ and 1.5 are considered. This suggests that as the central mass concentration increases

from $\gamma = 0$ to 1.5, the mechanism responsible for the formation of the symmetric two-armed nuclear spirals in barred galaxies shifts from the hydrodynamic shocks to the gas density waves. The symmetric two-armed nuclear spirals formed by hydrodynamic shocks in the models with $\gamma = 0$ drive a large amount of gas inflow than those explained by gas density waves in the models with $\gamma = 1.5$. Finally, we conclude that 2×10^4 SPH particles give the same results as 1×10^6 SPH particles, and thus are adequate to examine the shock nature of nuclear spirals in barred galaxies.

REFERENCES

Ann, H.B. 2001, AJ, 121, 2515

Ann, H.B., & Lee, H.M. 2004, ApJ, 613, L105

Ann, H.B., & Thakur, P. 2005, ApJ, 620, 197

Athanassoula, E. 1992, MNRAS, 259, 345

Balsara, D.S. 1995, J. Comput. Phys., 121, 357

Benz, W. 1990, in The Numerical Modelling of Nonlinear Stellar Pulsations, ed. J.R. Buchler (NATO ASI Ser. C 302; Dordrecht: Kluwer Academic), 269

Block, D.L., Puerari, I., Knapen, J.H., Elmegreen, B.G., Buta, R., Stedman, S., & Elmegreen, D.M. 2001, A&A, 375, 761

Buta, R.J., & Combes, F. 1996, Fund. Cosmic Phys., 17, 95

Carollo, C.M., Stiavalli, M., Seigar, M., de Zeeuw, P.T., & Dejonghe, H. 2002, AJ, 123, 159

Combes, F., Boisse, P., Mazure, A., & Blanchard, A. 2002, Galaxies and Cosmology (New York: Springer), 172

Cowei, L.L. 1980, ApJ, 236, 868

Dehnen, W. 1993, MNRAS, 265, 250

Elmegreen, D.M., Chromey, F.R., & Warren, A.R. 1998, AJ, 116, 2834

Elmegreen, B.G., & Thomasson, M. 1993, A&A, 272, 37

Englmaier, P., & Gerhard, O. 1997, MNRAS, 287, 57

Englmaier, P., & Shlosman, R.S. 2000, ApJ, 528, 677

Freeman, K.C. 1966, MNRAS, 134, 1

Freeman, K.C. 1970, ApJ, 160, 811

Fukuda, H., Habe, A., & Wada, K. 2000, ApJ, 529, 109

Fukuda, H., Wada, K., & Habe, A. 1998, MNRAS, 295, 463

Fux, R. 1999, A&A, 345, 787

Fux, R. 2001, JKAS, 34, 255

Hasan, H., Pfenniger, D., & Norman, C. 1993, ApJ, 409, 91

Hut, P., Makino, J., & McMillan, S. 1995, ApJ, 443, L93

Kamphuis, J. 1993, Ph.D. Thesis, Univ. Groningen

Knapen, J.H., Beckman, J.E., Heller, C.H., Shlosman, I., & de Jong, R.S. 1995, ApJ, 454, 623

Knapen, J.H. 1999, in the Evolution of Galaxies on Cosmological Timescales, ed. J.E. Beckman, & T.J. Mahoney (ASP Conf. Ser. 187), 72

Laine, S., Knapen, J.H., Perez-Ramiez, D., Doyon, R., & Nadeau, D. 1999, MNRAS, 302, L33

Laine, S., Knapen, J.H., Perez-Ramiez, D., Englmaier, P., & Matthias, M. 2001, MNRAS, 324, 891

Lee, C.W., Lee, H.M., Ann, H.B., & kwon, K.H. 1999, ApJ, 513, 242

Long, K., & Murali, C. 1992, ApJ, 397, 44

Maciejewski, W., Teuben, P.J., Sparke, L.S., & Stone, J.M. 2002, MNRAS, 329, 502

Maciejewski, W. 2003, in the Proc. JENAM 2002, Galactic and Stellar Dynamics, ed. C. Boily et al. (Les Ulis: EDP Sciences), 3

Maciejewski, W. 2004, MNRAS, 354, 892

Martini, P.,& Pogge R.W. 1999, AJ, 118, 2646

Martini, P., Regan, M.W., Mulchaey, J.S., & Pogge, R.W. 2003a, ApJS, 146, 353

Martini, P., Regan, M.W., Mulchaey, J.S., & Pogge, R.W. 2003b, ApJ, 589, 774

Monaghan, J. 1992, ARA&A, 30, 543

Namekata, D., Habe A., Matsui, H., & Saitoh, T.R. 2008, ApJ, Submitted (arXiv:0810.1095v1)

Patsis, P.A., & Athanassoula, E. 2000, A&A, 358, 45

Perez, I. 2008, A&A, 478, 717

Pfenniger, D., & Friedli, D. 1993, A&A, 270, 561

Phillips A.C., Illingworth, G.D., MacKenty, J.W., & Franx, M. 1996, AJ, 111, 1566

Piner, B.G., Stone, J.M., & Teuben, P.J. 1995, ApJ, 449, 508

Pogge R.W., & Martini, P. 2002, ApJ, 569, 624

Regan M.W., & Mulchaey J.S., 1999, AJ, 117, 2676

Selloow, J.A., & Wilkinson, A. 1993, Rep. Prog. Phys., 56, 173

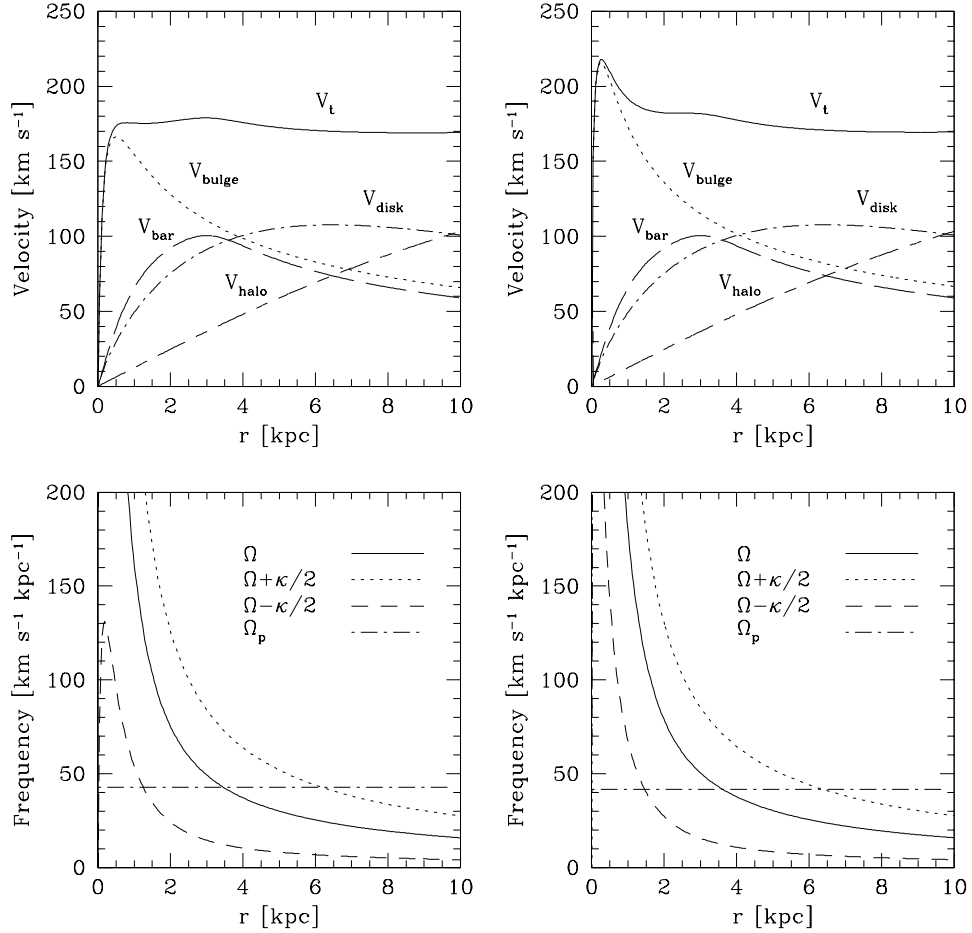Steinmetz, M. 1996, MNRAS, 278, 1005

Wada, K. 1994, PASJ, 46, 165

Fig. 1.— Rotation curves and angular frequencies of model galaxies. Because of the non-axisymmetric nature of the bar, its contribution is included here after averaging it axisymmetrically. Left: Model M1 with $\gamma = 0$; right: model M3 with $\gamma = 1$. The horizontal dot-dashed lines in the bottom panels represent the bar pattern speed of $\Omega_p = 42.8$ km s^{-1} kpc^{-1}.
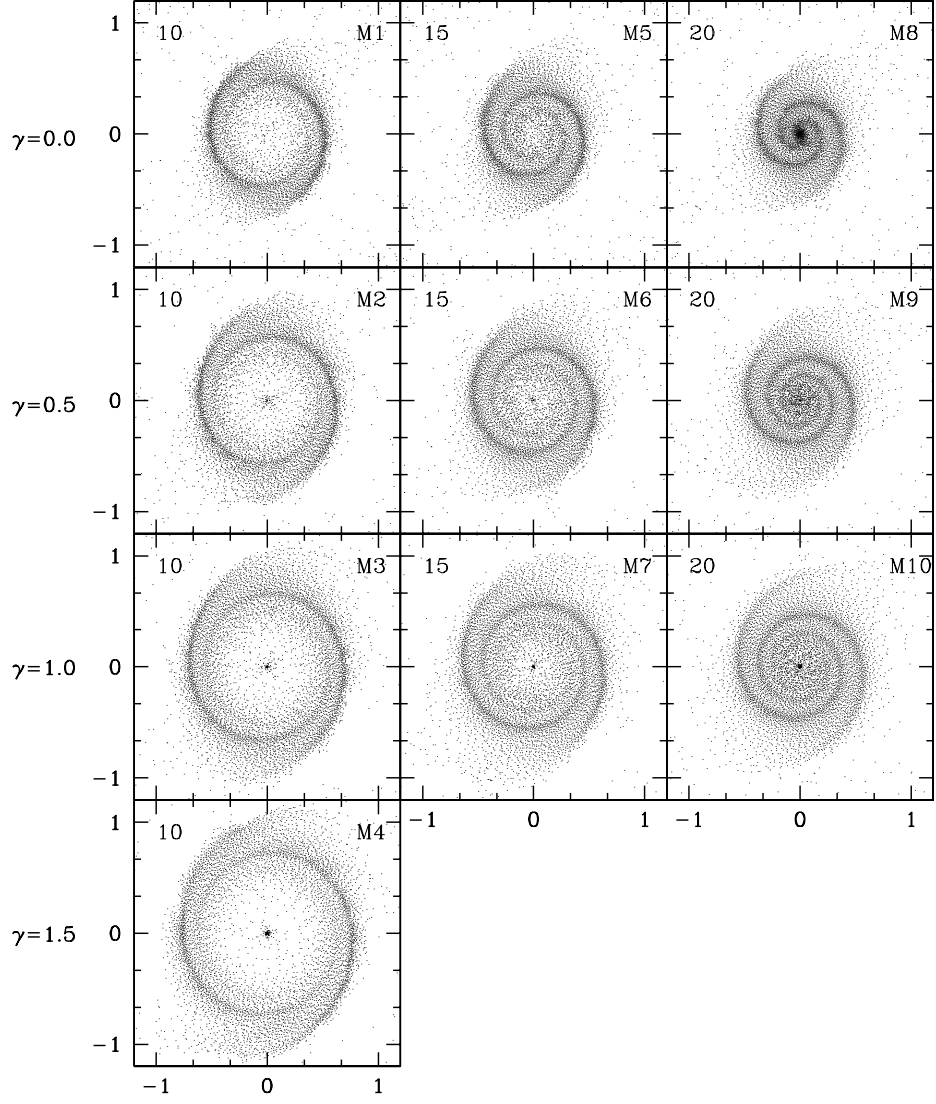
Fig. 2.— Nuclear features of the gaseous disks in models M1-M10 at the evolution time of $10\tau_{bar}$. The bar rotation period τ_{bar} is $\sim 1.44 \times 10^8$ yr. The models are indicated in the top right corner and the gas sound speed in units of kilometers per second is given in the top left corner of each panel. On the left side of each row, its corresponding value of the central mass concentration γ is given. The bar lies horizontally, and the box size is 2.4 kpc in one dimension.
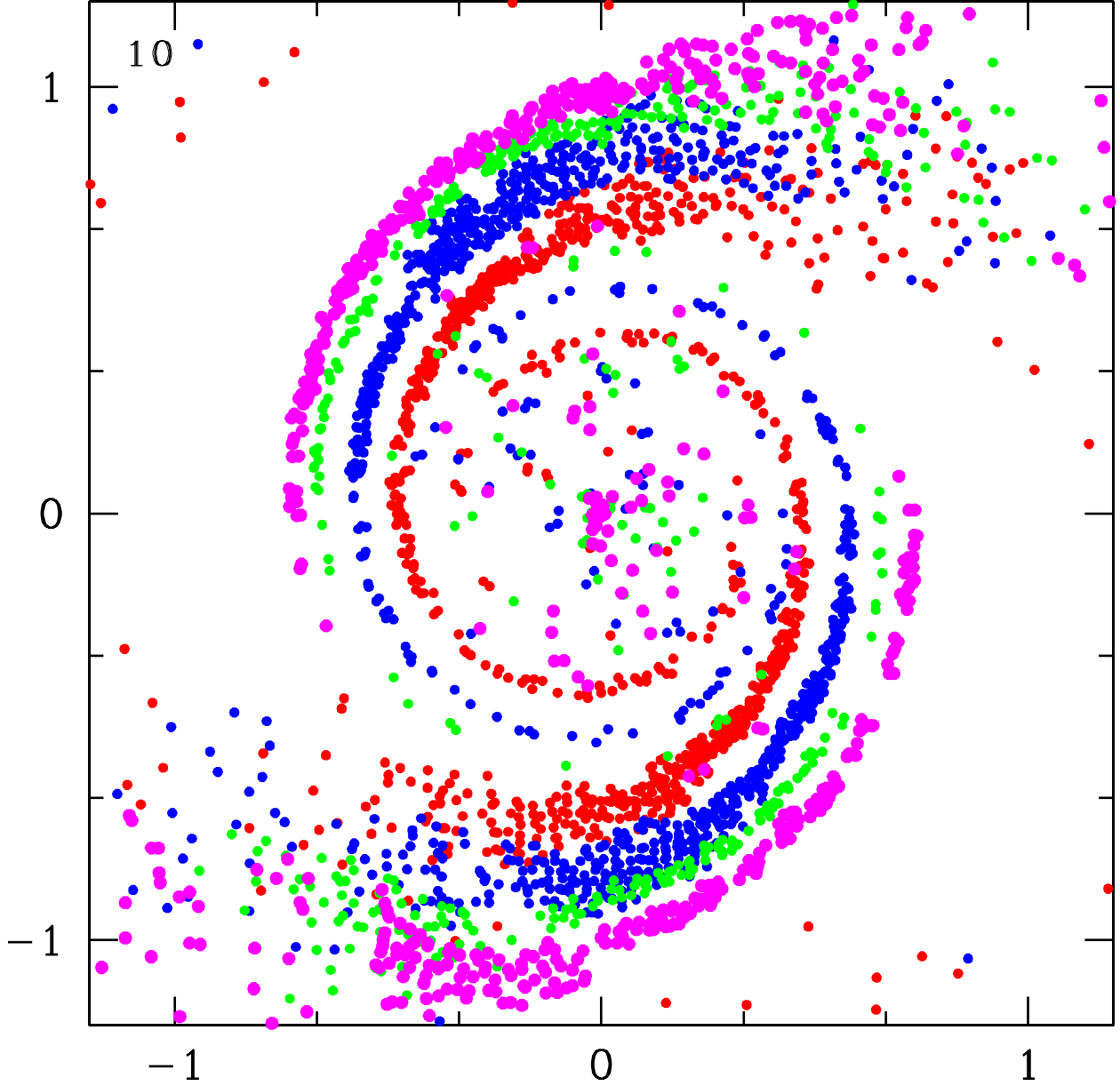
Fig. 3.— Nuclear distribution of the gas particles that are shocked by supersonic flow (i.e., $-h\nabla \cdot v > c_s$) for models M1-M4 at the evolution time of $10\tau_{bar}$. Red: model M1 with $\gamma = 0$; blue: model M2 with $\gamma = 0.5$; green: model M3 with $\gamma = 1$; magenta: model M4 with $\gamma = 1.5$. The gas sound speed is $c_s = 10$ km s^{-1}. The number in the top left corner of the panel is the evolution time in units of τ_{bar}. The bar lies horizontally, and the box size is 2.4 kpc in one dimension.
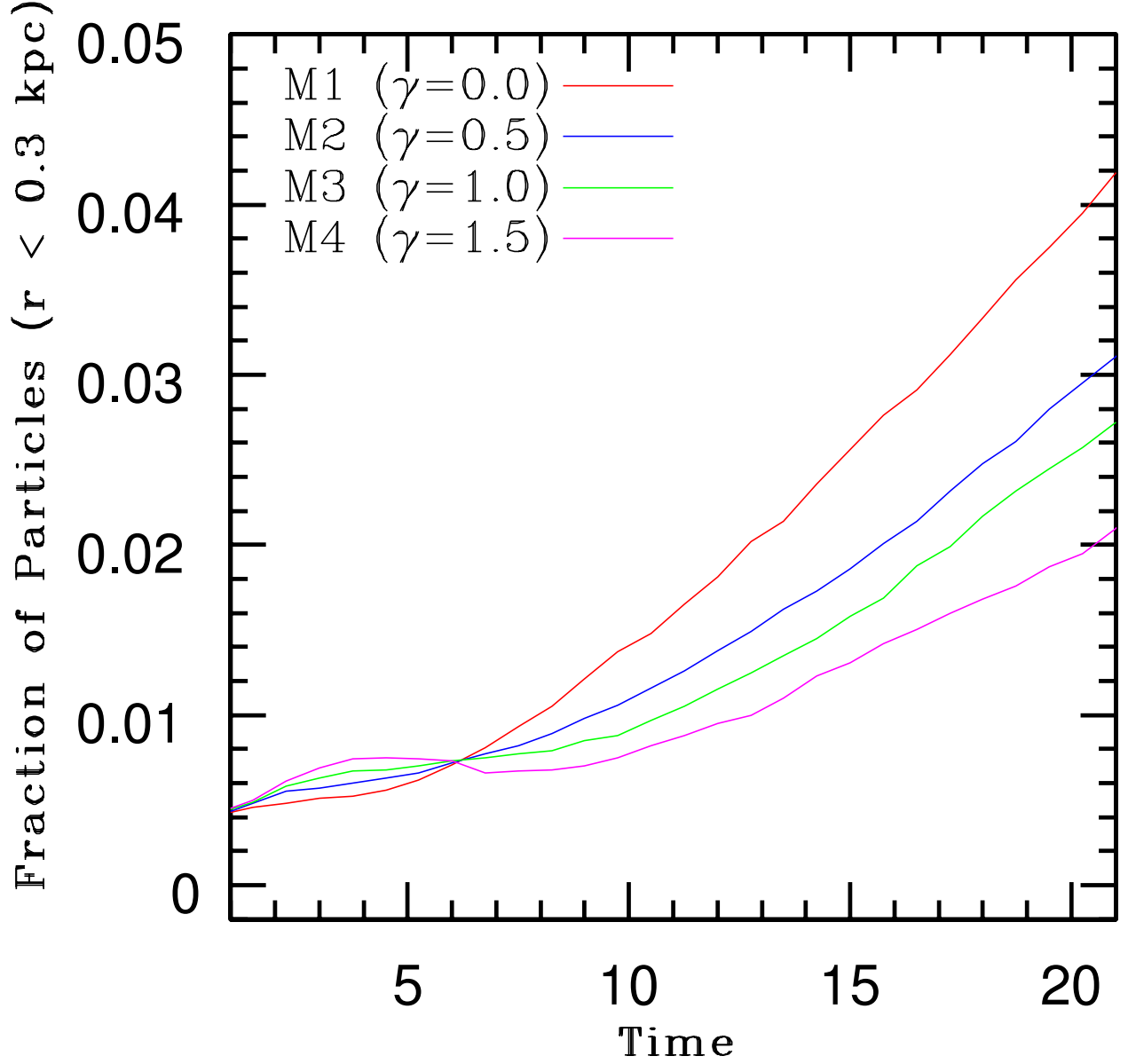
Fig. 4.— The inflow of the gas particle into the central hundred parsec of models M1-M4. The time evolution of the fraction of gas particles accumulated inside a radius of 0.3 kpc is shown. The time is given in units of τ_{bar}. The gas sound speed is $c_s = 10$ km s^{-1}. The line colors corresponding to each model are given in the top left corner of the panel.
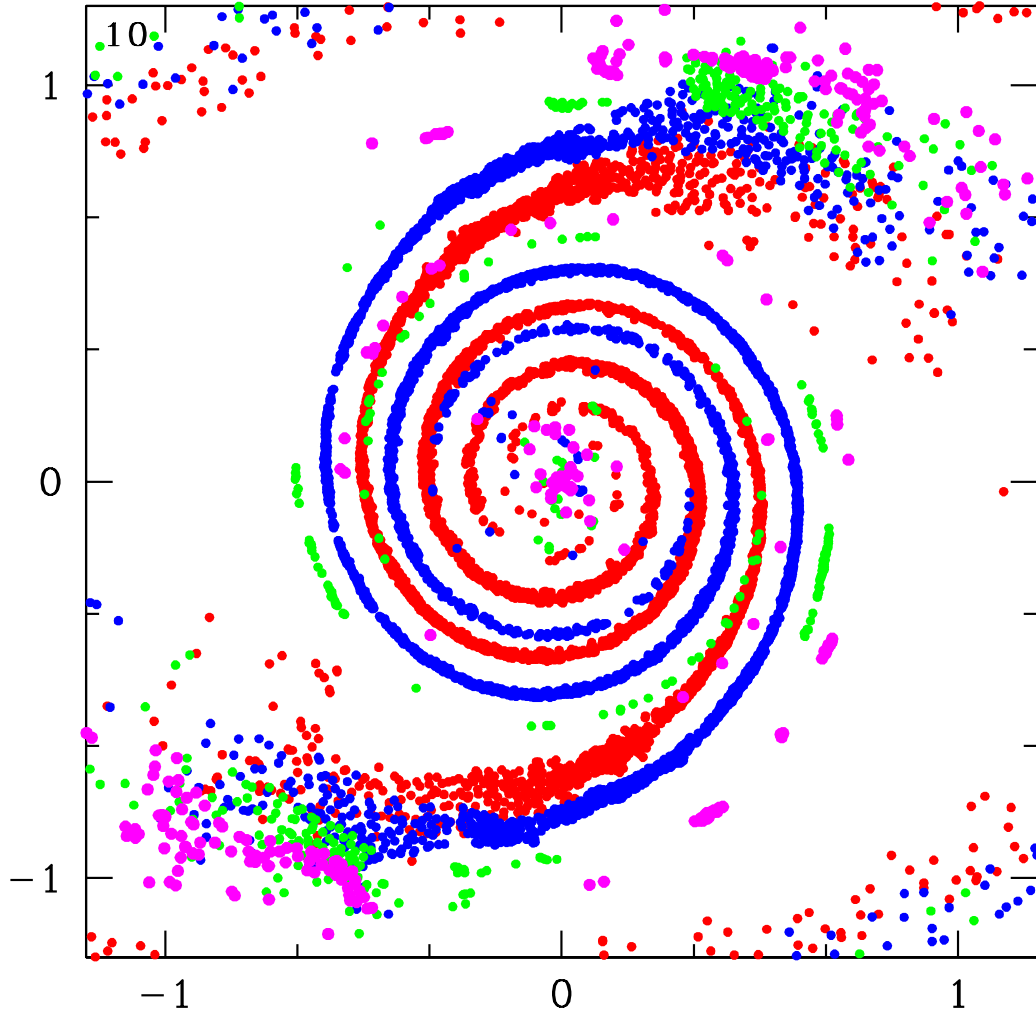
Fig. 5.— Same as Fig. 3, but for 1×10^6 SPH particles.